ELSEVIER

Contents lists available at ScienceDirect

Journal of Catalysis

journal homepage: www.elsevier.com/locate/jcat





Pentanuclear iron complex for water oxidation: Spectroscopic analysis of reactive intermediates in solution and catalyst immobilization into the MOF-based photoanode

Roman Ezhov ^a, Gabriel Bury ^a, Olga Maximova ^a, Elliot Daniel Grant ^a, Mio Kondo ^b, Shigeyuki Masaoka ^b, Yulia Pushkar ^a, ^{*}

ARTICLE INFO

Keywords: Water oxidation Electro catalysis X-ray absorption spectroscopy X-ray emission spectroscopy EPR Reaction mechanisms

ABSTRACT

Photoelectrochemical water splitting can produce green hydrogen for industrial use and CO2-neutral transportation, ensuring the transition from fossil fuels to green, renewable energy sources. The iron-based electrocatalyst $[Fe_4^{II}Fe_4^{II}(\mu-3-O)(\mu-L)_6]^{3+}$ (LH = 3,5-bis(2-pyridyl)pyrazole) (1), discovered in 2016, is one of the fastest molecular water oxidation catalysts (WOC) based on earth-abundant elements. However, its water oxidation reaction (WOR) mechanism has not been yet fully elucidated. Here, we present in situ X-ray spectroscopy and electron paramagnetic resonance (EPR) analysis of electrochemical WOR promoted by (1) in water-acetonitrile solution. We observed transient reactive intermediates during the in situ electrochemical WOR, consistent with a coordination sphere expansion prior to the onset of catalytic current. At a pre-catalytic (~+1.1 V vs. Ag/AgCl) potential, the distinct $g \sim 2.0$ EPR signal assigned to Fe^{III}/Fe^{IV} interaction was observed. Prolonged bulk electrolysis at catalytic ($\sim+1.6$ V vs. Ag/AgCl) potential leads to the further oxidation of Fe centers in (1). At the steady state achieved with such electrolysis, the formation of hypervalent Fe^V=O and Fe^{IV}=O catalytic intermediates was inferred with XANES and EXAFS fitting, detecting a short Fe \equiv O bond at ~ 1.6 Å. (1) was embedded into MIL-126 MOF with the formation of a (1)-MIL-126 composite. The latter was tested in photoelectrochemical WOR and demonstrated an increase in electrocatalytic current upon visible light irradiation in acidic (pH = 2) water solution. The presented spectroscopic analysis gives further insight into the catalytic pathways of multinuclear systems and should help the subsequent development of more energy- and costeffective water-splitting catalysts based on earth-abundant metals. Photoelectrocatalytic activity of (1)-MIL-126 confirms the possibility of creating an assembly of (1) inside a solid support and harnessing solar irradiation towards industrial applications of the catalyst.

1. Introduction

Hydrogen is the most potent energy carrier and chemical fuel crucial for decarbonization of the world's economy and mitigating climate change and global warming. As of 2021, 76 % of hydrogen is produced from natural gas by steam methane reforming, 22 % is produced through coal gasification, and only 2 % from water electrolysis. [1] Green hydrogen production is a clean and sustainable energy technology based on the concept of artificial photosynthesis. This concept suggests utilization of renewable electricity (solar panels, wind turbines, etc.) for water electrolysis using conventional electrolyzers, as well as the

engineering of a single device combining light absorption and charge-separation functionality with water-splitting catalysis. [2–5] The realization of artificial photosynthesis requires fast and durable water-splitting catalysts, capable of promoting the most challenging multi-electron water oxidation reaction (WOR) step: $2H_2O \rightarrow O_2 + 4e^- + 4H^+$, with subsequent proton reduction reaction for hydrogen production. For technologically viable and scalable artificial photosynthesis processes, the catalyst must be embedded within a solid support, and the use of any toxic or flammable reagents should be minimized. Metal organic frameworks (MOFs) provide outstanding chemical flexibility and tunability of physical properties and thus, can be envisioned as

E-mail address: ypushkar@purdue.edu (Y. Pushkar).

^a Department of Physics and Astronomy, Purdue University, West Lafayette, IN 47907, USA

^b Division of Applied Chemistry, Graduate School of Engineering, Osaka University, 2-1 Yamadaoka, Suita, Osaka 565-0871, Japan

^{*} Corresponding author.

integration scaffolds for light-induced water splitting. [6-8]

The slow kinetics of WOR result in high noble metal (Ru and Ir) loadings in commercial electrolyzers, making their use expensive and non-scalable. By contrast, the Mn₄Ca center of Photosystem II (PS II) allows conversion of sunlight to stored chemical energy with $\sim 60 \ \%$ efficiency, using only the earth-abundant Mn and Ca atoms. [9–11] This demonstrates that efficient catalytic systems can be achieved using earth-abundant materials. The Mn₄Ca cluster of PS II inspired substantial research and development of artificial WOCs based on 3d transition metals. [12-17] For advanced design and development of a water oxidation catalyst (WOC), the knowledge of the reaction mechanisms and catalytic pathways is crucial. This motivates development of catalysts with decreased reaction overpotential to improve energy conversion efficiency. Avoiding the use of precious metals to promote WOR is also important for scalability and broader industry applications beyond hydrogen production, such as oxidative transformations in organic synthesis. Currently, the noble metal WOCs (Ru- and Ir-based) provide the most effective and stable water-splitting catalysis. [18.19] Their catalytic pathways were studied thoroughly (Fig. 1A) and may provide guidance for WOR catalysts based on earth-abundant metals (Fig. 1B,C). Mechanisms related to the metal intermediates in high oxidation states are proposed for artificial WOCs, where PCET results in the formation of metal-oxo species M = O (M - transition metal), followed by water nucleophilic attack (WNA) or radical coupling with the formation of transient (hydro)peroxides, further oxidation, and the subsequent release of oxygen (Fig. 1D). [20-23] In some cases, it was possible to

observe the reactive intermediates in freeze-quenched reaction mixtures in single and bi-metallic WOCs - (Fig. 1A, C) [22,24,25] or *in situ* in electrochemical WOR for a multinuclear catalyst (Fig. 1B) [23]. Highly oxidized transient species have been detected for Ru-based WOCs, [20,21,26] as well as for a few WOCs based on earth-abundant metals. [22,27–29] The presence of Fe^V intermediates for the representative [Fe (pytacn)]²⁺ WOC was also postulated, and [Fe^V=O,OH(pytacn)]²⁺ was experimentally detected in the chemically driven WOR. [22,30,31] While the formation of Fe^{IV} and Fe^V is considered to be a common phenomenon for WOR promoted by iron-based WOCs, reports of spectroscopically characterized Fe^V catalytic species are rare. [22,29,32–34].

The study of reaction pathways for multinuclear clusters represents a significant challenge due to the system complexity and short lifetime of the reactive intermediates. Here, EPR analysis will consider the strong electronic couplings of metal centers, and X-ray spectroscopy will report the average charge state for metal ions in the WOC. The Mn₄Ca cluster of PS II is the most-studied example, where the S₃ state of the oxygen evolving complex (OEC) is characterized by a Mn₄^{IV} state. [35–37] OEC also includes the essential Ca²⁺ cofactor; when Ca²⁺ is depleted, oxygen evolution by the OEC is halted. Higher oxidation states of Mn, such as Mn^V, were proposed for the S₄ state based on DFT models; [38,39] however, such proposals currently lack substantial enough experimental evidence to fully support the presence of higher oxidation states such as Mn^V or Mn^{VI}. Models involving Mn^V formation in the S₄ state also fail to resolve the kinetic challenge posed by the similar rates of Tyr₂^{*} reduction

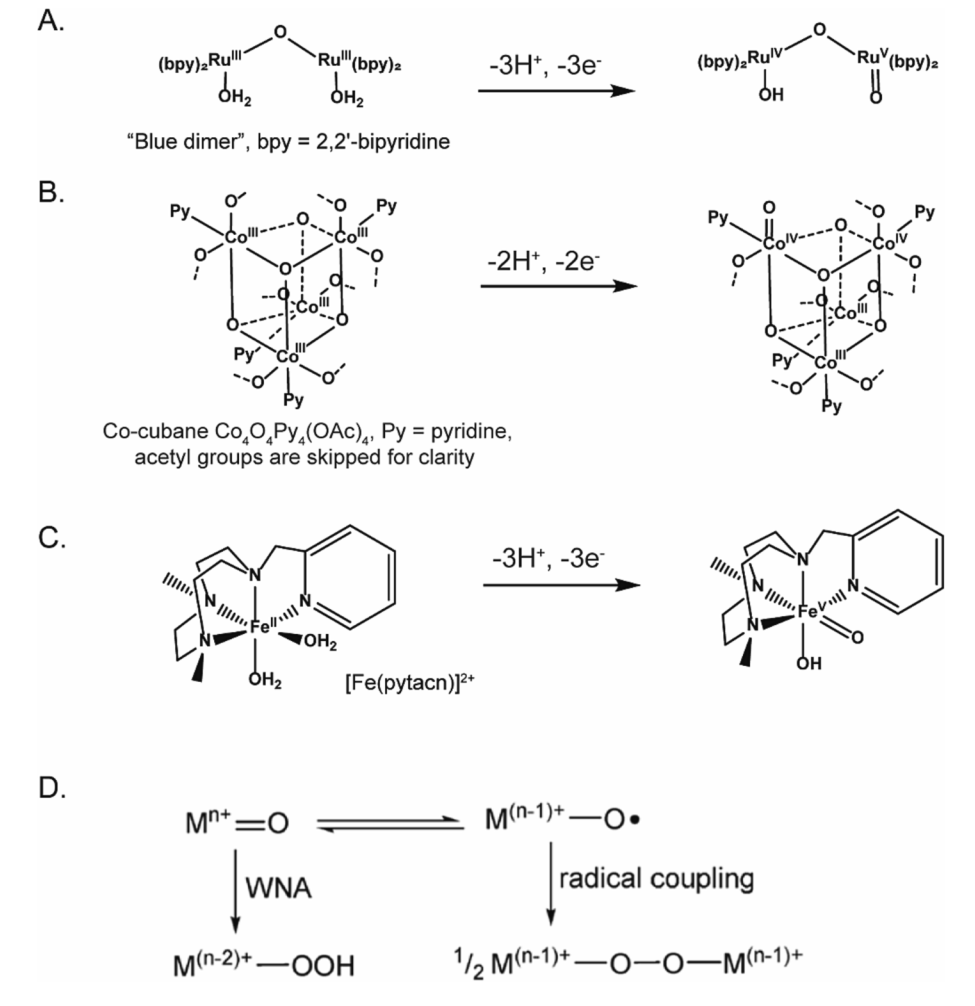


Fig. 1. Formation of the reactive metal-oxo species intermediates in chemical (A [24], C [22]) and electrochemical (B [23]) WOR promoted by molecular catalysts. The M = O (M - transition metal) species can undergo water nucleophilic attack or combine via radical coupling, resulting in [O-O] moiety formation, further oxidation, and dioxygen evolution (D).

and O_2 evolution. [11,37] Some catalytically inactive Mn/Ca/O clusters mimics were reported, [40] but active WOCs are usually monometallic (Fig. 1B, Fig. 2). Artificial monometallic Co- and Fe-based clusters demonstrate noticeable stability in electrocatalytic water oxidation but do not precisely mimic the natural heterometallic CaMn₃O₄. [41]

Here, we report in situ spectroscopic characterization of WOR promoted by $[Fe_4^{II}Fe_4^{III}(\mu-3-O)(\mu-L)_6]^{3+}$ (LH = 3,5-bis(2-pyridyl)pyrazole) (1) (Fig. 2A), with support of X-ray emission spectroscopy (XES), X-ray absorption spectroscopy (XAS), and EPR. This catalyst mediates electrochemical water oxidation in acetonitrile-water solution with a turnover frequency measured to be $\sim 1900~\text{s}^{-1}$ at $\sim +1.4~\text{V}$ vs. Fc⁺/Fc (~+1.6 V vs. Ag/AgCl). [14] In the trigonal bipyramidal metal core of (1), a planar Fe₃O fragment is sandwiched with two apical hexacoordinated [Fe(µ-L)₃] moieties. All Fe ions in the Fe₃O core are pentacoordinated, indicating the potential for coordination sphere expansion. Electrochemical analysis in acetonitrile indicates four redox processes preceding the onset of catalytic water oxidation. [42] Structural transformations explaining WOR activity of (1) (Fig. 2A) were proposed based on DFT calculations. [43] A mechanism with the formation of adjacent Fe^{IV}=O species (Fig. 2B, Fig. 1-high), followed by O-O bond formation via radical coupling (Fig. 2B, (1)-O-O) and subsequent oxygen evolution was presented. [43] This proposal is different from the WNA mechanism suggested for a Co-cubane WOC based on spectroscopic analysis. [14,44] For the latter, recently reported spectroscopic analysis indicated generation of Co^{IV}=O and hydroperoxo Co-OOH moieties during WNA before the oxygen release. [23,45] Similarly to the Co multinuclear analogue, the WNA electrocatalytic pathway for (1) cannot be excluded, and the WOR mechanism promoted by (1) may also be reevaluated with the input of advanced spectroscopic techniques. In this study, we analyze electrocatalytic pathway for (1) using in situ synchrotron-based X-ray spectroscopy and EPR.

We recently demonstrated the capability of the Fe-based MIL-126 metal organic frameworks (MOFs) doped with a Ru-based WOC to oxidize water photoelectrochemically under visible light and moderate potential. [46] The Fe₃O nodes in the MOF are capable of forming charge-separated states upon visible light irradiation. This promotes WOR and increases the electrocatalytic current. [46,47] These considerations encouraged us to assemble the water oxidation composite bearing (1) inside a MIL-126 MOF; we then tested its activity in an acidic water solution (pH = 2, required for the use of Nafion as proton transport layer) under intense visible light. The (1)-MIL-126 composite is electrocatalytically active at + 1.6 V vs. Ag/AgCl applied potential at pH = 2 in water and displays sensitivity to visible light with \sim 3 times higher electrocatalytic current than control MIL-126 MOF.

2. Results

2.1. Electronic structure characterization of (1) by X-ray emission spectroscopy (XES)

The initial state of (1) has an intriguing electronic structure which was first analyzed by Mossbauer spectroscopy at low temperature and was reported to consist of two low-spin (LS) Fe^{II} ions, two high-spin (HS) Fe^{II} ions, and one Fe^{III} ion in HS state. [48] To validate that this electronic structure remains at room temperature, we recorded Fe K_{β} X-ray emission spectra [49] of (1) from a powder pellet at room temperature and under a cryostream (see Materials and Methods, SI). These spectra contain information about the Fe centers' oxidation state and spin state. [50–52] The XES spectra of (1) is significantly broader than the spectra of reference compounds containing single-type Fe ions (Fig. 3, Figure S1). The XES spectrum of (1) can be successfully modeled by the superposition of XES spectra for FeSO₄ (Fe^{II}, HS), ferrocene Fe(C₅H₅)₂ (Fe^{II}, LS), and Fe₂O₃ (Fe^{III}, HS) in a ratio of 2:2:1, as is shown in Fig. 3. This result confirms the electronic structure assignment and shows that Fe K_B XES can be used for analysis of Fe-based WOC intermediates. The spectra modeled as a superposition of XES spectra of standard compounds with different ratios are provided in Figure S2. The spectra

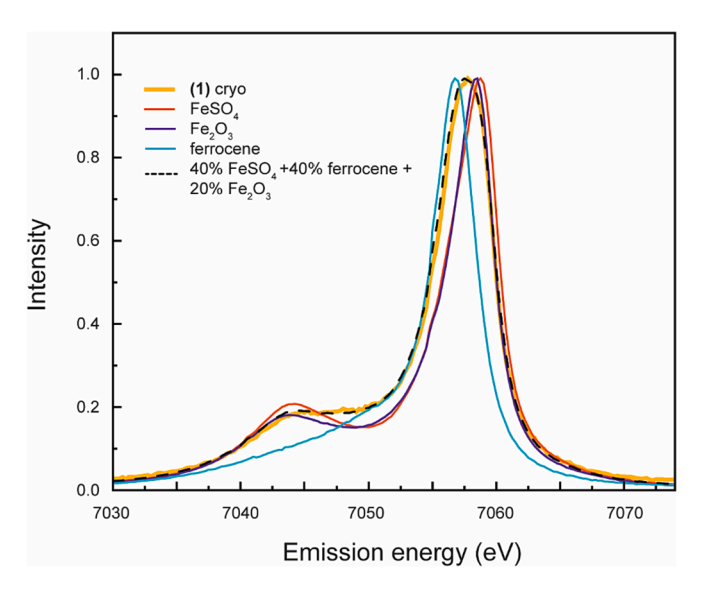


Fig. 3. Fe K_β XES spectra of powder pellet of (1) (yellow) and modeled XES spectrum (black dashed line) obtained as superposition of FeSO₄ (Fe^{II}, HS), ferrocene (Fe^{II}, LS), and Fe₂O₃ (Fe^{III}, HS) spectra in a ratio of 2:2:1. All K_β XES spectra were normalized to a maximum after a linear background was subtracted across the energy range of 7020 to 7080 eV by fitting the first and last ten data points in the range. (For interpretation of the references to colour in this figure legend, the reader is referred to the web version of this article.)

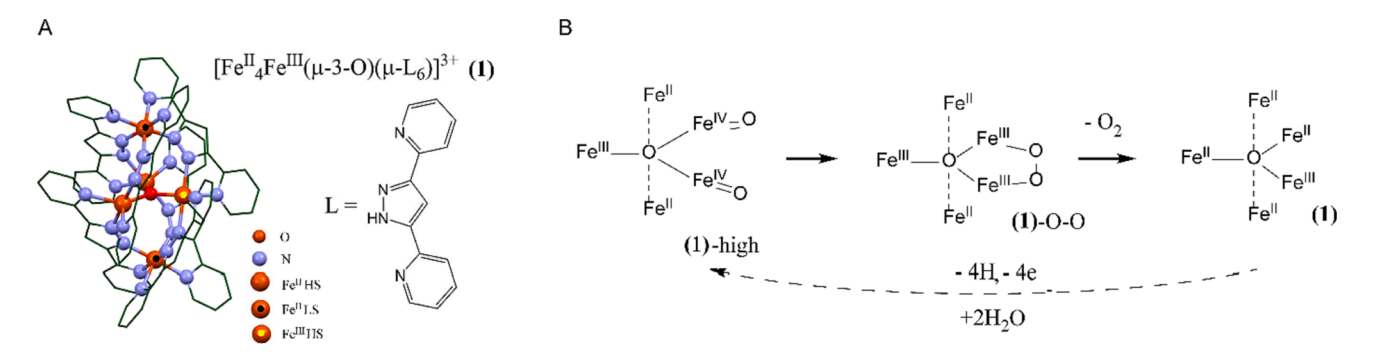


Fig. 2. A) Pentanuclear Fe-based water oxidation electrocatalyst (1), oxidation and spin states of Fe centers (HS – high-spin, LS – low-spin) are indicated; B) Key steps of the catalytic cycle proposed based on DFT analysis of μ-oxo iron core of (1) during electrochemical WOR.

obtained for similar cases of 2:1:2 and 1:3:1 for Fe^{II}(HS): Fe^{II}(LS): Fe^{III}(HS) do not match the experimental data highlighting the sensitivity of XES technique to electronic configuration of metal ions (see **Figure S2**). XES will be used in the future for *in situ* measurements of Febased WOCs preserved in a suitable cryostate or generated in electrochemical cells compatible with an XES spectrometer. [49]

2.2. In situ XAS study of electrochemically driven WOR catalyzed by (1) in solution

For better understanding of the electrocatalytic reaction pathways, it is important to study metastable chemical species generated in situ under applied potential. [23,53-56] Bulk electrolysis (BE) of 0.2 mM solution of (1) was performed at + 1.6 V vs. Ag/AgCl reference electrode (corresponding to the catalytic current at + 1.42 V vs. Fc/Fc⁺) [14] in a 1:4 water-acetonitrile mixture, with addition of 0.1 M Et₄NClO₄ as the supporting electrolyte (pH = 6), while stirred in a closed cell to prevent acetonitrile evaporation. The custom electrochemical cell was equipped with a Pt-foil working electrode as an anode, Pt-wire counter electrode placed in a fritted tube filled with same electrolyte (0.1 M Et₄NClO₄ in acetonitrile-water mixture), and a Ag/AgCl reference electrode (Figure S3). Since the pH of the solution in the cell during prolonged BE shifts to more acidic due to high catalyst activity (H⁺ generation as a result of WOR) and the electrolyte's lack of buffer capacity (note corresponding pH increase in the fritted tube with the counter electrode), pH was checked after every third XAS scan and was adjusted to pH \sim 6–7, as necessary. During prolonged electrolysis (>8 h at + 1.6 V vs. Ag/ AgCl), we observed a gradual shift of the Fe K-edge in XANES (Fig. 4.A, B) rightwards from the Fe₂O₃ standard, signifying that the average oxidation state of the Fe₅ core exceeds Fe^{III}, Fig. 4B. We note that XANES reflects an average oxidation state of the 5 Fe atoms, and it is impossible to differentiate oxidation states of individual Fe centers. No signs of catalyst degradation - such as precipitate or thin film formation inside the electrochemical cell or on the Pt electrode surface - were noted. At about ~ 5 h of BE, the XANES edge does not shift further, indicating a steady-state condition equivalent to the catalytic WOR conditions. At the conclusion of the in situ XAS experiment, the cell window material and electrode were rinsed and subjected individually to the XRF analysis at the beamline and demonstrated a lack of Fe signal.

Fig. 4B shows that *in situ* XANES of (1) at + 1.6 V vs. Ag/AgCl is positioned about $\sim 1/3$ in between the Fe₂O₃ and [Fe^V=O,OH (pytacn)]²⁺. [22] Assuming $\sim 100 \%$ Fe^{III} and Fe^V for two comparison spectra and linear dependence of edge position with charge of the iron center, one can derive Fe^{III}₂Fe^{IV}₃ or Fe^{III}₃Fe^V₁Fe^V configuration for electrolyzed (1). However, Fe^{III}₃Fe^{IV}₂ cannot be excluded due to approximate nature of such analysis. For multinuclear metallic clusters, it is appropriate to assume a linear relationship between the edge position and the oxidation state of metal ions as no dramatic changes in the ligand environment are expected which can influence edge position. This approach was used for the Mn₄Ca cluster in Photosystem II, [57] a Co₄O₄ cubane WOC, [23] and other spectroscopic works referenced in these.

A comparison of the EXAFS spectrum of initial (1) and that obtained at catalytic steady-state at $\sim+1.6$ V νs . Ag/AgCl is shown on Fig. 4C; EXAFS fits are in Table S1-2. The peak corresponding to the first coordination sphere of Fe increases in intensity and shifts to the lower apparent distance (marked with the arrow). Fitting of the EXAFS data indicates formation of a five-coordinated reactive species bearing an ultrashort Fe-O distance of ~ 1.56 Å (Fig. 4C, Table S2, Figure S4). While XANES data cannot univocally distinguish between the Fe2 Fe3 and Fe3 Fe1 Fe V configurations, the obtained Fe=O distance is more consistent with Fe V formation, [22,58] as Fe1 O distances are expected to be longer, at 1.62-1.66 Å. [59,60] Per reviewer request, we conducted DFT calculations using the BP86/Def2TZVP to explore the energy of Fe3 Fe1 Fe1 O \rightarrow Fe3 Fe1 Fe1 O \rightarrow Fe3 Fe1 O \rightarrow Fe3 Fe1 O \rightarrow Fe3 Fe1 O \rightarrow

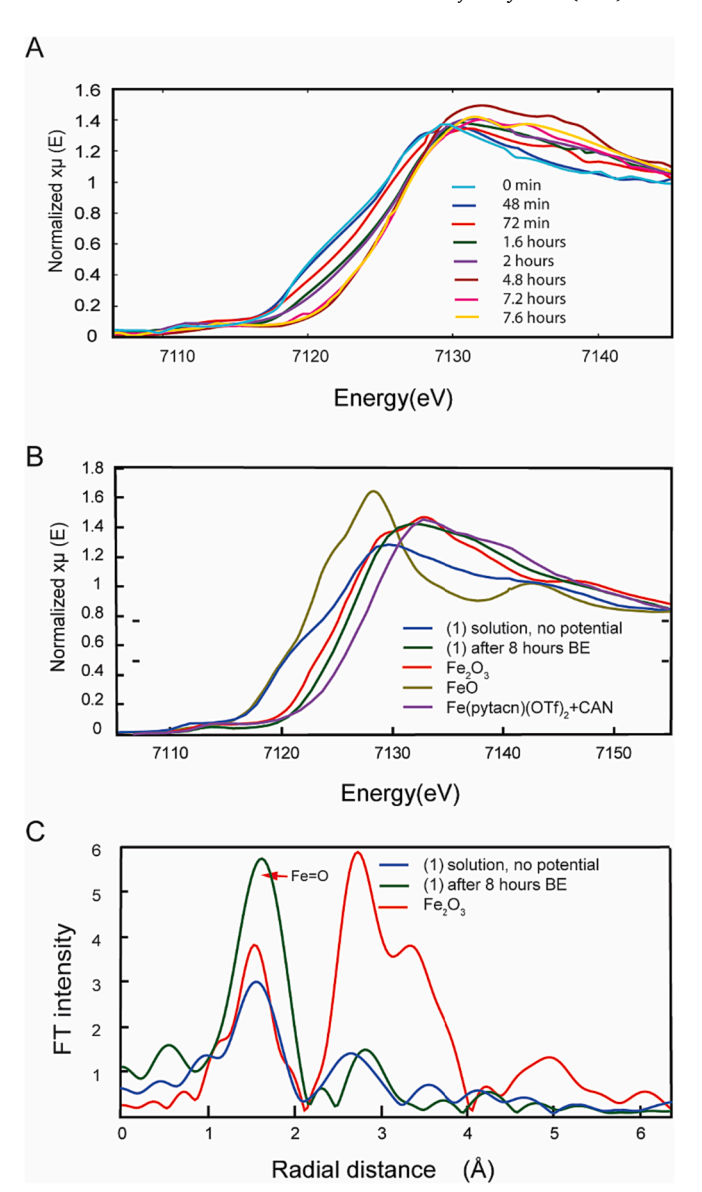


Fig. 4. A) Dynamic of XANES change for the separate scans of (1) solution in 4:1 acetonitrile – water mixture during prolonged BE at + 1.6 V vs. Ag/AgCl; B, C) Comparison of XANES (B) and EXAFS (C) of (1) after prolonged BE, with standards ((1) initial, FeO, and Fe $_2$ O $_3$) and highly oxidized Fe $_2$ V obtained by chemical oxidation of the Fe(pytacn)(OTf) $_2$ complex with cerium (IV) ammonium nitrate at pH = 1.

Scheme 1 [43] and further optimized each state, Table S3; note DFT-computed potentials are given vs. NHE, while experimental electrochemical potentials are reported vs. Ag/AgCl. We found $\sim\!+1.2$ V vs. NHE for the Fe^IIIFe^IV=O \rightarrow Fe^IVFe^IV=O transition – likely insufficient for Fe^IVFe^IV=O to activate water. In the next step, Fe^IVFe^IV=O \rightarrow Fe^IVFe^V=O is predicted at + 1.80 V vs. NHE, in agreement with the high onset potential for this catalyst. We conclude that within the precision limits of DFT – typically \pm 0.2 V – formation of the Fe^V=O species is possible.

2.2.1. EPR studies

The initial complex (1) consists of two low-spin (LS) Fe^{II} ions, two high-spin (HS) Fe^{II} ions, and one Fe^{III} ion in the HS state, Fig. 2A. The solution of 0.2 mM (1) in a 1:4 water – acetonitrile mixture with 0.1 M Et_4NClO_4 as an electrolyte was found to be EPR silent at 20 K (Fig. 5A) – the initial species lacks strong EPR signal or is high spin and not detectable due to fast relaxation or transitions outside the X-band range.

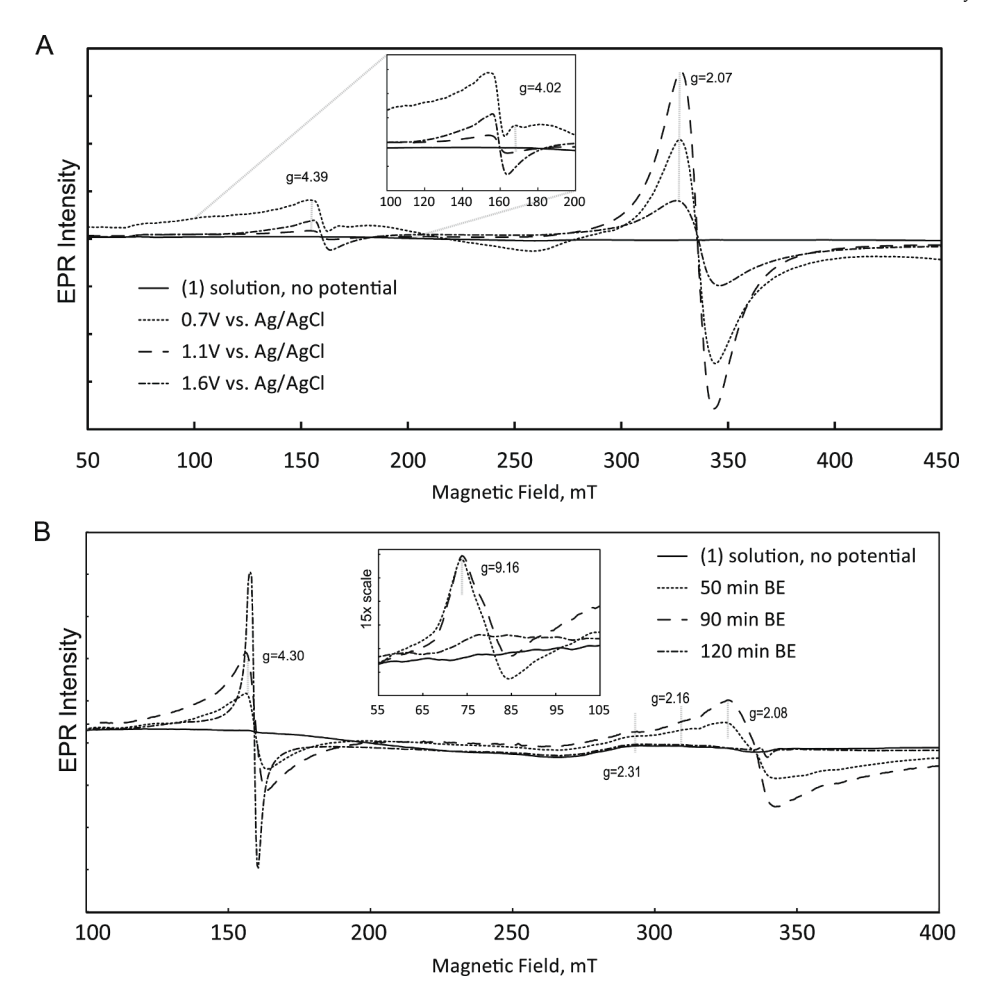


Fig. 5. X-Band EPR of (1) electrolyzed: A) at increasing potential for 1 h at each potential, B) at fixed potential of +1.6 V vs. Ag/AgCl reference electrode at different time points. Samples were flash frozen in liquid N_2 for cryogenic EPR analysis. Modulation amplitude is 25 G, Temperature is 20 K, and microwave power is 31 mW.

While in situ XAS was performed only at the catalytic applied potential of + 1.6 V vs. Ag/AgCl due to the limited availability of the beamtime, EPR was explored at multiple applied potentials; bulk electrolysis conditions for EPR studies match the conditions used for in situ XAS. The following redox processes at + 0.3, +0.7, +1.2 V νs . Fc⁺/Fc were reported to correspond to $Fe_3^{II}Fe_2^{III} \to Fe_2^{II}Fe_3^{III} \to Fe_4^{III} \to Fe_5^{III}$ transitions in an aprotic environment. [14] Bulk electrolysis at + 0.7 V vs. Ag/AgCl reference electrode (this is above the $\sim +0.3$ V vs. Fc⁺/Fc) is expected to oxidize the two remaining Fe^{II} centers in the Fe₃O planar fragment to Fe^{III}, producing the Fe₂^{II}Fe₃^{III} configuration. [14] EPR of the resulting solution shows signals at g \sim 2.00 and g \sim 4.23; here "g" refers to the g-factor, a descriptor of a paramagnetic feature unique to electronic structures. The signal at g $\sim 4.2\bar{3}$ is typical of high-spin Fe $^{III}.$ [61–63] Thus, the appearance of $g \sim 4.23$ signal is expected. However, the g \sim 2.0 signal is even more intense, and its width of \sim 200 G indicates that it originates from a metal center rather than organic radical. Fe^{II} centers with a 6-coordinate nitrogen ligand environment are known to oxidize to Fe^{III} state at relatively high redox potentials; for instance, $Fe(bpy)_3^{2+}$ would need + 1.06 V vs. SHE (+0.83 V vs. Ag/AgCl). [64] We argue that Fe centers coordinated to the oxygen in the planar core Fe₃O of the complex, rather than the two "axial," nitrogen-coordinated Fe centers, would be first to oxidize. The observed g ~ 2.0 signal can potentially originate from the antiferromagnetic coupling of Fe^{III} centers in Fe₃O planar core, lowering the total spin and generating an S=1/2signal, but other mechanisms are also possible, as discussed below. Please note that two iron centers outside the Fe₃O plane are low spin and reside at a significant distance (~4.5 Å) from three more tightly coupled ions of the Fe₃O plane.

Increasing the potential to +1.1 V vs. Ag/AgCl (above the +0.7 V vs. Fc⁺/Fc) results in the growth of the g \sim 2.00 signal, and the total transferred charge was estimated at ~ 3e more oxidized, compared to the initial (1). Thus, for the state at $\sim +1.1$ V vs. Ag/AgCl, we can expect Fe^{II}Fe^{III} or Fe^{II}Fe^{III}Fe^{IV} charge configurations. Three high-spin Fe^{III} ions can potentially result in a state with S=1/2, but examples of $g\sim 2.0$ EPR spectral features are unknown in the literature for the combination of three high-spin Fe^{III} ions. However, spin-coupling between Fe^{III} and Fe^{IV} is known to result in EPR signals with g \sim 2.0. [65] The so-called "intermediate X" in Ribonucleotide reductase R2 has been previously assigned to contain high-spin ferric $S = 5/2 \text{ Fe}^{III}$ species coupled to highspin Fe^{IV} (S = 2), resulting in an S = 1/2 spin system with a signal at g ~ 2.0, though this specific signal has a narrow linewidth, ~20 G. [66] Fe^{III}/Fe^{IV} -coupled systems with Fe^{IV} triplet spin state (S = 1, resulting in total spin S = 3/2) have been studied through EPR spectroscopy. [67–69] The most prominent feature in these is a narrow line with $g_{xx} =$ 4.03. Such a feature is not observed in our spectra, though when (1) is oxidized for 120 min at + 1.6 V vs. Ag/AgCl (+1.2 V vs. Fc⁺/Fc), a unique, narrow feature is produced with $g_{xx}=4.30$. In a separate experiment, sampling the solution during the electrolysis at fixed + 1.1 V vs. Ag/AgCl shows an increase of the g \sim 2.0 EPR signal (Figure S6) under the same conditions but does not produce the $g \sim 2.0$ EPR feature in the absence of water (Figure S7). Thus, we assign the $g \sim 2.0$ signal to the Fe₅ core with insertion of at least one water molecule. Such insertion can be in the form of water, -OH, or oxo ligand on one of equatorial plane 5-coordinate Fe, expanding its coordination to 6-coordinate. To test stability of paramagnetic states, the intermediate formed from (1) oxidized at + 1.1 V vs. Ag/AgCl was measured by cryogenic X-Band EPR

spectroscopy, before and after melting for five minutes, **Figure S8**. The species producing gFactor ~ 2 EPR signal is short lived at room temperature, and its amplitude reduces by ~ 80 % in just 5 min. This might indicate the presence of reactive Fe^{IV} center in the species responsible for strong g ~ 2 EPR signal able to be generated at intermediate + 0.7 to + 1.1 V applied potential.

Increasing oxidizing potential to + 1.6 V vs. Ag/AgCl (above the + 1.2 V vs. Fc⁺/Fc) results in the decrease of g \sim 2.00 signal (Fig. 5A, B). Thus, the more oxidized state is likely EPR silent. Sampling the solution at different time points during electrolysis (Fig. 5B) at fixed + 1.6 V vs. Ag/AgCl shows increase in the g \sim 4.23 signal with longer oxidation. However, g \sim 2.0 does not build up substantially under such conditions, with a maximum magnitude at 90 min, likely due to its reactivity. The g \sim 9.0 signal may be assigned to an additional high spin intermediate. Despite the possibility of Fe^V being present, as suggested by the XANES experiment, we do not expect an Fe^V EPR signal characteristic for the single-site Fe^V state, due to coupling of multiple Fe centers in the cluster.

2.2.2. Photoelectrocatalytic activity of (1) embedded in a solid support of MIL-126 MOF

We previously demonstrated that visible light-generated chargeseparated states in the u-oxo Fe₃O nodes of MIL-126 metal organic framework (MOF) have sufficient oxidizing potential to enable electrocatalytic WOR of the $[Ru(bpy)(dcbpy)(H_2O)_2]^{2+}$ (bpy = 2,2'-bipyridine, dcbpy = 2,2'-bipyridine-5,5'-dicarboxylic acid) at pH = 1 with the onset potential $\sim +1.6$ V vs. NHE, when incorporated as a linker in the MOF structure. [46] However, it was not clear if Fe₃O nodes can drive a WOC with a higher onset potential of $\sim +1.8$ V vs. NHE when trapped inside the MOF, as opposed to when incorporated as a linker in the MOF structure. Incorporation of large molecules like (1) inside the MOF pores requires large pore volumes and relatively long linkers. Taking into account the approximate size of (1) (about 12×15 Å, Cambridge Crystallographic Data Center CCDC #996195¹⁴) and the average pore size in MIL-126 10×11 Å [70], entrapment of (1) inside the pores of MIL-126 seems possible in a tightly packed crystalline structure, with a locally distorted linker environment around catalyst molecules. [71,72] Synthesis of the (1)-MIL-126 assembly was realized by a standard solvothermal synthesis procedure. [46,73] While 10 % and higher mass content of (1) in the composite material leads to the formation of a poorly crystalline phase, the mass proportion ~ 8 % of (1) does not interfere with the well-established crystalline structure of MIL-126, as verified by PXRD (Figure S9A). The presence of unchanged (1) incorporated in MIL-126 was confirmed using UV-vis and mass spectrometry upon the dissolution of the (1)-MIL-126 composite (Figure S9B, C). We

noted that MIL-126 dissolves in 1 M borate buffer (pH = 7), likely due to the substitution of carboxylate linkers by boric acid. This allowed us to digest (1)-MIL-126 in the buffer and analyze the extract for the presence of the intact (1). UV–vis of the extract reveals similar to (1) peak pattern due to bis(pyridyl)pyrazolate ligand absorption lines around the μ -oxo Fe₅O core (Figure S9B). Mass spectrometry of digested (1)-MIL-126 followed by extraction with dichloromethane shows a similar fragmentation pattern as the starting molecular complex (1) (Figure S9C).

The photoanode (1)-MIL-126-FTO was fabricated by the drop casting of the (1)-MIL-126 mixture with a Nafion ionomer on FTO electrode surface (see Materials and Methods). Its photo-response in 0.01 M nitric acid was measured as reported earlier in 3-electrode electrochemical cell, with the (1)-MIL-126 as a photoanode, Pt wire as a counter electrode, and Ag/AgCl as a reference electrode (Fig. 6A). [46] To assess the photo response, the light/dark sequence was applied - 11 light/dark cycles (1 min light/1 min dark) – during application of + 1.6 V vs. Ag/ AgCl potential to the photoanode (jagged path of the curves). At pH = 2under visible light, (1)-MIL-126 shows ~ 3 times increase in photocatalytic current, compared to blank MIL-126 in the control experiment (Fig. 6B) at +1.6 V vs. Ag/AgCl applied potential. As seen from Fig. 6B, (1)-MIL-126-FTO has a more prominent photo response compared to Fe MIL-126 without (1) catalyst. At lower pH, the curve of electrocatalytic current becomes erratic, likely due to instability of (1) in acidic media. [74] From this perspective, the fabricated (1)-MIL-126 photoanode demonstrates the validity of the "ship-in-the-bottle" approach to implement the molecular catalyst into a water-splitting light-activated device.

3. Discussion

Studying artificial catalytic systems inspired by Nature [75,76] with *in situ* spectroscopic characterization combined with computational analysis is crucial for better understanding and developing of rational designs of artificial catalytic systems. [77,78] Such a combined approach can reveal reaction pathways and transformations of a catalyst aiding the rational development of a better catalytic system. The two most notable multinuclear electrocatalytic systems reminiscent of the natural PS II photosynthetic complex reported to date are Co-cubane $Co_4O_4Ac_4Py_4$ [79] and (1). Thus, it is hard to overestimate the importance of knowledge about their reaction mechanisms.

Earlier, the state corresponding to $[Fe^{II}Fe^{II}_{4}(\mu-3-O)(\mu-L)_{6}]^{6+}$ was obtained by BE at + 1.19 V vs. Ag/AgCl, in acetonitrile, with no water present. It was assigned based on Mossbauer and UV–vis characterization as one Fe^{II} , two low-spin Fe^{III} , and two high-spin Fe^{III} . [48] This

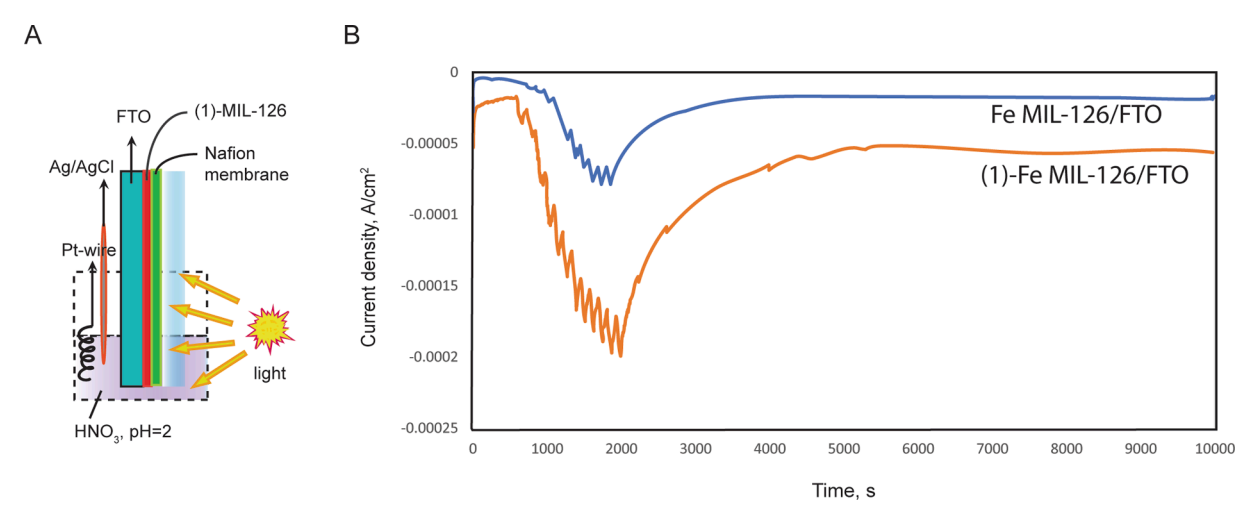


Fig. 6. Photoelectrocatalytic activity of (1)-MIL-126 photoanode (orange curve) in comparison with the Fe MIL-126 drop casted on FTO (blue curve) at +1.6 V vs. AgCl/Cl applied potential. 11 light/dark cycles (1 min light/1 min dark) were applied to the activated electrode assembly (denoted by jagged path of the curves). (For interpretation of the references to colour in this figure legend, the reader is referred to the web version of this article.)

result is in agreement with our EPR analysis of samples electrolyzed at + 1.1 V vs. Ag/AgCl in pure acetonitrile, where only the EPR signal with g \sim 4.3 was detected, in agreement with the presence of Fe^{III} centers (Figure S7). High-spin Fe^{III} is well-characterized by EPR features with g-Factor \sim 4.3. [61–63] The same electrolysis with 20 % of additional water present, however, results in a new $g \sim 2$ EPR signal (Fig. 5A, S6). This signal appears as early as when $\sim 3e^{-}$ are removed at + 1.1 V vs. Ag/ AgCl. The closest similar signal in the literature is from the so-called "intermediate X" in Ribonucleotide reductase R2 and implies $\mathrm{Fe^{IV}}\text{-}\mathrm{Fe^{III}}$ interaction. [66] We speculate that new $g \sim 2.0$ EPR signal indicates a coordination sphere expansion at an oxidation state below Fe₅^{III} and subsequent proton coupled electron transfer (PCET) facilitated oxidation to Fe^{IV}-Fe^{III} state. EPR analysis of the (1) oxidized in the acetonitrile without water shows a lack of the $g \sim 2.0$ signal, indirectly confirming our proposal. Per Siegbahn analysis, [43] water insertion into Fe^{II}Fe^{III} to generate Fe^{II}Fe^{III}W is associated with a barrier of 19.0 kcal/mol, and this step is endergonic by 16.3 kcal/mol. Further deprotonation of Fe^{II}Fe₄^{III}W is exergonic by 7.8 kcal/mol, as its pKa was calculated to be - 0.9. Taken together, the first water binding and deprotonation process for Fe^{II}Fe^{III}₄ is endergonic by 8.5 kcal/mol, while same process for a more oxidized Fe₅^{III} state is endergonic by 1.2 kcal/mol. [43] The driver for the formation of the water insertion intermediate might be its subsequent PCET oxidation. The $g \sim 2$ intermediate is likely present in a mixture with other species; thus, we did not attempt its EXAFS analysis. Per EPR analysis, the $g \sim 2$ intermediate is not present at a catalytic steady state, likely due to its further oxidation.

Earlier attempts to characterize catalytic species of (1) during WOR indicated formation of iron oxide on the glassy carbon electrode. [74] While usage of oxidizable materials in highly oxidative reaction media seems to be controversial, in our experimental approach we used Pt electrode as the working electrode. This minimized side reactions, such as interaction of WOR-generated highly reactive species with an electrode material, delivering reliable data for *in situ* XAS and EPR. No precipitate formation or thin film deposition was observed during BE with the Pt electrode.

Our in situ XANES and EXAFS analysis demonstrated oxidation of (1) in the presence of water to $Fe_3^{III}Fe^{IV}Fe^{V}$ or $Fe_2^{III}Fe_3^{IV}$ configuration as a solution steady-state at $\sim+1.6$ V vs. Ag/AgCl. Earlier DFT analysis suggested that Fe₃^{III}(Fe^{IV}=O)₂ state can accomplish O-O bond formation via radical coupling with $\sim+8.8$ kcal/mol barrier. [43] The Fe^{IV}=O distance was computed to be ~ 1.61 Å, which is close to measured here by EXAFS, ~ 1.56 Å. EXAFS data are consistent with a Fe^V=O group, but Fe^{IV}=O cannot be excluded based on the EXAFS fits alone. We also cannot determine the number of Fe=O groups based on EXAFS alone, due to high uncertainty with N numbers in EXAFS fits. The presence of 1-2 Fe=O groups agrees with EXAFS results (Table S2). The detected highly oxidized iron centers may undergo radical coupling (see Fig. 7), as proposed in the theoretical scheme by Siegbahn et al. [43] However, the water nucleophilic attack (WNA) with subsequent formation of peroxo- species cannot be excluded, similar to the other Fe- and Cobased WOCs reported earlier. [23] To initiate WNA, a Fe^V=O center would likely be required, similar to other earth-abundant-metal-based WOCs like Fe(pytacn)²⁺, Fe(TAML)²⁺, and Co cubane. [22,23,80,81] While the $Co^{IV} = O$ state might be sufficiently energetic to activate water, a single $Fe^{IV} = O$ was shown not to be active in WNA.

While comprehensive mechanistic insight of electrocatalytic water oxidation is essential, the importance of catalyst implementation into a system toward industrial application is hard to overestimate. Since chemical immobilization of (1) inside MIL-126 was not possible due to lack of a suitable ligand, the "ship-in-the-bottle" technique of the catalyst encapsulation was carried out. [71,82] This approach suggests assembly of a metal organic framework around the well-defined object (nanoparticle or molecule) of interest and was used for fabrication of catalytic NP-MOF, drug- and enzyme-MOF composites. [83–85] Encaging of [(terpy)Mn(μ -O)₂Mn](terpy)]³⁺ into MIL-101(Cr) was reported, [86] but we later demonstrated that Cr-MIL is unstable under

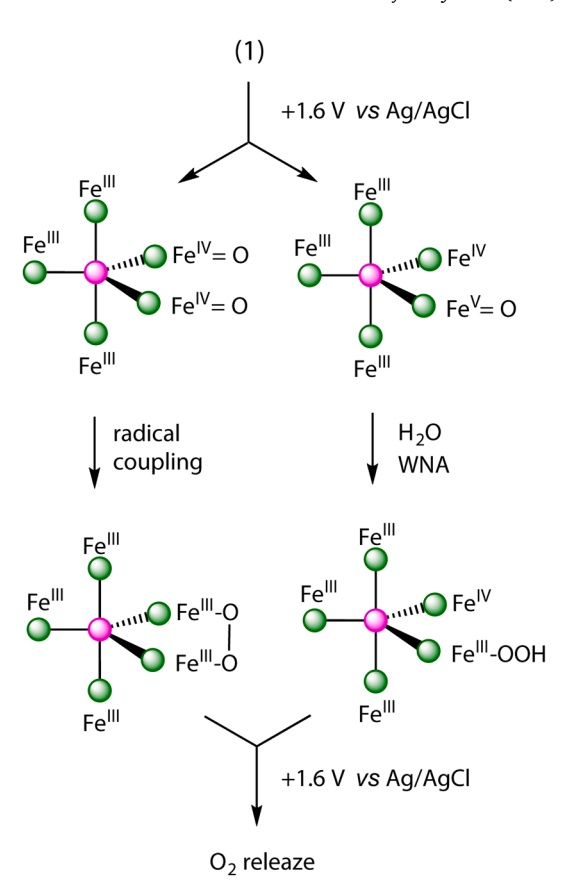


Fig. 7. Schematic representation of catalytic intermediates in WOR most consistent with *in situ* XAS data. Two reaction pathways with participation of high-valent Fe species are depicted: radical coupling (Fe^{IV} formation) and water nucleophilic attack (WNA, Fe^V formation). The actual number of highly oxidized species in the catalyst molecule may differ as well as a final state of the complex after oxygen release.

condition of WOC due to fast oxidation of Cr^{III} (unpublished results). We trapped (1) within a metal organic framework (Fe MIL-126) using the "ship-in-the-bottle" approach and realized its catalytic performance without a toxic solvent (acetonitrile) in water acidic media (pH = 2). Moreover, the obtained system demonstrated a photo response improving its catalytic current with visible light irradiation. Currently, the performance of (1)-MIL-126 system is lower than the that reported for Ru(bpy)(dcbpy)(H2O)2-Fe-MIL-126 composite, due to higher onset potential of (1) relative to the Ru-based [Ru(bpy)(dcbpv)(H₂O)₂1²⁺. The low photocurrent can be attributed to low electrical conductivity of MIL-126 MOF (3.3 \times 10⁻⁹ S/cm) in which (1) was embedded, the limited lifetime of the excited state of Fe₃O nodes of MIL-126 upon photon absorption, [46] and the possibly limited electron transfer between the incapsulated (1) and photoexcited nodes. Future improvements in Febased WOC should help to achieve performances matching the family of Ru-based catalysts.

4. Conclusions

Hypervalent Fe^V=O and Fe^{IV}=O catalytic intermediates are implicated in multiple oxidative reactions, including electrochemical water oxidation. To date, despite ample experimental effort, detection of these species in electrocatalytic WOR, promoted by multinuclear catalyst (1), has been corroborated indirectly. *In situ* XAS reveals transient highvalent metal species during electrochemical water splitting catalyzed by (1), thus confirming previous mechanistic considerations about the coordination sphere expansion of the in-plane Fe centers promoting water oxidation. During *in situ* bulk electrolysis of water in water-

acetonitrile solution of (1) at catalytic potential we observed: 1) a gradual shift of Fe $_5$ core K-edge toward more oxidized state beyond Fe $^{\rm III}$ in XANES, and 2) EXAFS data revealing the presence of an ultrashort Fe=O distance of ~ 1.56 Å. A spin state of (1) consistent with Fe $^{\rm III}$ /Fe $^{\rm IV}$ -coupled systems was observed by EPR of the reaction mixture during BE at the potential (+1.1 V vs. Ag/AgCl) below the onset of catalytic current. The composite (1)-MIL-126 material was shown to function as a photoanode at pH = 2. The presented results provide further insight towards the development of multinuclear water oxidation catalysts based on earth-abundant metals and their application in economically viable technological schemes for clean and sustainable hydrogen production.

5. Materials and methods

5.1. General information

All chemicals and solvents were purchased from Sigma Aldrich and TCI America, and they were used as received. (1) was obtained from Prof. Masaoka (Osaka University). Additional amounts of (1) were prepared according to [14]. Aqueous solutions were prepared using ultrapure (Type 1) water (resistivity 18.2 M Ω -cm at 25 °C) from Q-POD unit of Milli-Q integral water purification system (Millipore, Billerica, MA, USA). PXRD data were collected using a Panalytical Empyrean Powder X-ray diffractometer. Mass spectrometry was performed using an Advion mass spectrometer. All electrochemical experiments were conducted using a potentiostat (CHI 627C; CH Instruments Inc., Austin, TX, USA).

5.1.1. EPR spectroscopy

X-band EPR measurements were performed on an EMX X-band spectrometer equipped with an X-Band CW microwave bridge (Bruker, Billerica, MA, USA). Samples were electrolyzed under reported conditions and frozen in liquid nitrogen within 30 s. During EPR measurements, the sample temperature was maintained at the reported temperature using a closed-cycle cryostat (ColdEdge Technologies, Allentown, PA, USA). Spectrometer conditions were as follows: microwave frequency 9.47 GHz, field modulation amplitude 25 G at 100 kHz, microwave power 31 mW, unless otherwise mentioned. Measurements were performed on the same day in the same conditions, to allow accurate comparison of signal intensities. A sample (\sim 0.2 ml) of electrolyzed solution was taken from the electrochemical cell and quickly (within 2 s) frozen in liquid N₂.

5.2. Preparations

5.2.1. Synthesis of (1)-MIL-126

A mixture of 360 mg of ferric chloride hexahydrate (1.33 mmol), 160 mg of 4,4′-biphenyl dicarboxylic acid (0.66 mmol), 13 mg of (1) (0.007 mmol), and 80 μ L of acetic acid in 20 ml of DMF was heated at 140° C for 48 h. Then the reaction mixture was cooled, and dark orange crystals were filtered from colorless solution, washed with DMF and acetone, and dried. Yield: 160 mg.

5.2.2. Photoanode fabrication

Photoelectrode fabrication using drop casting of catalytically active MOFs (DC-electrodes) was performed according to the reported procedure. [46,87] For each electrode, 4 mg of (1)-MIL-126 was suspended in 0.5 ml of isopropanol with addition of 8 μL of Nafion solution (5 % in alcohol/water, Sigma Aldrich Inc.). Second, the suspended mixture obtained was layered on an FTO electrode surface, and we waited until almost complete evaporation of isopropanol to deposit successive layers. Five layers of the suspended MOF mixture were deposited. After drop casting, the MOF-bearing electrodes were dried on air at room temperature.

5.3. Electrochemical experiments

5.3.1. Bulk electrolysis of (1) in water-acetonitrile mixture

Bulk electrolysis (BE) was accomplished using 0.2 mM solution of (1) in 10 ml of 0.1 M Et₄NClO₄ electrolyte in acetonitrile – water (4:1 ratio) in a custom-made 3-electrode cell for in situ XAS, while a glass beaker was used for all other experiments. Platinum foil was used as the working electrode, platinum wire in a frit served as the counter electrode, and a saturated Ag/AgCl electrode acted as the reference electrode. The pH of the solutions in the main compartment and the fritted tube was monitored after every three XAS scans (every ~ 1.5 h), adjusting pH to neutral with 1 M NaOH solution in the cell or with 1 M nitric acid solution in the frit, as necessary. BE of (1) in acetonitrile was done with 0.2 mM solution of (1) in 10 ml of acetonitrile with 0.1 M LiClO₄ solution as electrolyte. Platinum foil was used as the working electrode, platinum wire in a fritted tube with the electrolyte solution (0.1 M LiClO₄ in acetonitrile) served as the counter electrode, and a saturated Ag/AgCl electrode acted as the reference electrode. At the conclusion of the in situ XAS experiment, the cell wall and electrode were rinsed and subjected individually to the XRF analysis at the beamline, demonstrating a lack of Fe signal.

5.3.2. Photolectrochemistry of (1)-MIL-126 MOF

Photoelectrochemical experiments were conducted using standard single-compartment 3-electrode cell. The FTO electrodes were electrically contacted using the uncoated FTO layer and masked to a geometrical surface area of 1 cm². A drop-casted MOF photoanode was firmly covered by a proton-conductive Nafion membrane, and the bottom of the assembly was submerged into 0.01 M nitric acid solution (pH = 2). A piece of platinum wire served as the counter electrode, and a saturated Ag/AgCl electrode served as the reference electrode. Anodes were illuminated with an unfocused 500 W light source \sim 25 cm away from the sample; the light passed through UV-filter/IR filter (\sim 2 cm of CuSO4 water solution).

All reported measurements were repeated several times to ensure the reproducibility of results.

5.4. X-ray emission spectroscopy (XES)

The Fe K_B XES data were collected at the Advanced Photon Source (APS) at Argonne National Laboratory on insertion device beamline 20-ID. At 20-ID, the radiation was monochromatized by a Si(111) doublecrystal monochromator. Focusing was done using Rh-coated KB mirrors, operated at 4 mrad grazing incidence. A He-filled chamber (I0) with a beam cleanup pinhole was placed before the sample to monitor the intensity of the incident X-rays. The energy of the incident beam was selected using monochromator, calibrated by setting the first inflection of an iron foil to 7112 eV. The incident monochromator was then set to an excitation energy of 7.3 keV to non-resonantly excite the sample. The beam-spot size was 100 \times 100 $\mu m^2,$ and the photon flux was $2{\cdot}10^{13}$ photons/s. For data collection, we used a home-built spectrometer [88] (energy resolution ~ 0.2 eV) based on a diced von Hamos design with accessing LiNbO3 (1,-5,-6) crystal analyzers reflections and a 150 eV collection range containing the $K\beta'$, $K\beta_{1,3}$ emission peaks. The spectra were recorded onto a two-dimensional position-sensitive detector (2D-PSD) Pilatus 100 k by Dectris and processed using AXEAP software.

5.5. XAS and EXAFS measurements

X-ray absorption spectra were collected at the Advanced Photon Source (APS) at Argonne National Laboratory on bending magnet beamline 20 at electron energy 23 keV and average current of 100 mA. The radiation was monochromatized by a Si(110) crystal monochromator. The intensity of the X-rays was monitored by three ion chambers (I_0 , I_1 , and I_2) and placed before the sample (I_0) and after the

sample (I_1 and I_2). I_1 , I_2 , and I_3 were filled with 100 % nitrogen. The X-ray energy was calibrated by setting the first maximum in the derivative of the Fe metal K-edge XANES spectrum to 7112 eV. The *in situ* electrochemical cell had a Kapton tape window on the X-ray beam path, forming a 45° angle relative to the X-ray beam and detector. Data were recorded as fluorescence excitation spectra using a 13-element energy-resolving detector. To reduce the risk of sample damage by X-ray, the defocused mode (beam size 1×7 mm) was used, and no damage nor precipitate formation were observed.

5.6. DFT calculations

The DFT optimizations were performed by Gaussian 16 with unrestricted BP86 Becke's 1988 functional [90] and the gradient corrections of Perdew [91]. The basis set def2tzvp was used for all atoms, unless noted otherwise. The CPCM polarizable conductor model was used to model water solvation. DFT calculations were performed on species relevant to redox reactions, Table S3. Redox potentials of reactions, shown in Table S3, were computed based on the energies of these optimized structures; note that uncertainty of DFT-based estimates for redox potentials is typically \pm 0.2 V. The value of the reference potential (RHE) was assigned to 4.44 V and redox potentials are reported for reaction at pH = 0. [92] Our group validated this precision for many Rubased water oxidation catalysts, where exact assignment of the redox species to electrochemical processes is available. [92–94] Other groups validate this approach for Fe-based systems [30,43] with the value of the reference potential (SHE) assigned to 4.28 V in pure water (4.68 V for reaction at pH = 0).

Declaration of competing interest

The authors declare that they have no known competing financial interests or personal relationships that could have appeared to influence the work reported in this paper.

Data availability

Data will be made available on request.

Acknowledgments

This research was supported by NSF, CHE-2155060 (Y.P.), by GM132024 (T32 Molecular Biophysics Training Program to G.B.) from the National Institute of General Medical Sciences (NIGMS), and by JSPS KAKENHI (22K21348) and JST CREST (JPMJCR20B6), Japan (S.M.). The use of the Advanced Photon Source, an Office of Science User Facility operated by the U.S. Department of Energy (DOE) Office of Science by Argonne National Laboratory, was supported by the U.S. DOE under Contract DE-AC02- 06CH11357. The PNC/XSD (Sector 20) facilities at the Advanced Photon Source and research at these facilities were supported by the U.S. Department of Energy, Basic Energy Science and the Canadian Light Source. Access to EPR was provided by the Amy Instrumentation Facility at Purdue University, Department of Chemistry, under the supervision of Dr. Michael Everly and Dr. Aloke Bera.

Appendix A. Supplementary material

Supplementary data to this article can be found online at https://doi.org/10.1016/j.jcat.2023.115230.

References

- [1] M.H. McCay, S. Shafiee, 22 Hydrogen: An Energy Carrier, in: T.M. Letcher (Ed.), Future Energy, (Third Edition), Elsevier:, 2020, pp. 475–493.
- [2] B. Zhang, L. Sun, Artificial photosynthesis: opportunities and challenges of molecular catalysts, Chem. Soc. Rev. 48 (7) (2019) 2216–2264.

- [3] S. Cestellos-Blanco, H. Zhang, J.M. Kim, Y.-X. Shen, P. Yang, Photosynthetic semiconductor biohybrids for solar-driven biocatalysis, Nat. Catal. 3 (3) (2020) 245–255
- [4] M. Kondo, H. Tatewaki, S. Masaoka, Design of molecular water oxidation catalysts with earth-abundant metal ions, Chem. Soc. Rev. 50 (12) (2021) 6790–6831.
- [5] D.K. Dogutan, D.G. Nocera, Artificial Photosynthesis at Efficiencies Greatly Exceeding That of Natural Photosynthesis, Acc. Chem. Res. 52 (11) (2019) 3143–3148.
- [6] P. Horcajada, F. Salles, S. Wuttke, T. Devic, D. Heurtaux, G. Maurin, A. Vimont, M. Daturi, O. David, E. Magnier, N. Stock, Y. Filinchuk, D. Popov, C. Riekel, G. Férey, C. Serre, How Linker's Modification Controls Swelling Properties of Highly Flexible Iron(III) Dicarboxylates MIL-88, J. Am. Chem. Soc. 133 (44) (2011) 17839–17847.
- [7] A.E. Baumann, D.A. Burns, B. Liu, V.S. Thoi, Metal-organic framework functionalization and design strategies for advanced electrochemical energy storage devices, Commun. Chem. 2 (1) (2019) 86.
- [8] H. Furukawa, K.E. Cordova, M. O'Keeffe, O.M. Yaghi, The Chemistry and Applications of Metal-Organic Frameworks, Science 341 (6149) (2013) 1230444.
- [9] H. Dau, M. Haumann, The manganese complex of photosystem II in its reaction cycle—Basic framework and possible realization at the atomic level, Coord. Chem. Rev. 252 (3) (2008) 273–295.
- [10] J. Kern, R. Chatterjee, I.D. Young, F.D. Fuller, L. Lassalle, M. Ibrahim, S. Gul, T. Fransson, A.S. Brewster, R. Alonso-Mori, R. Hussein, M. Zhang, L. Douthit, C. de Lichtenberg, M.H. Cheah, D. Shevela, J. Wersig, I. Seuffert, D. Sokaras, E. Pastor, C. Weninger, T. Kroll, R.G. Sierra, P. Aller, A. Butryn, A.M. Orville, M. Liang, A. Batyuk, J.E. Koglin, S. Carbajo, S. Boutet, N.W. Moriarty, J.M. Holton, H. Dobbek, P.D. Adams, U. Bergmann, N.K. Sauter, A. Zouni, J. Messinger, J. Yano, V.K. Yachandra, Structures of the intermediates of Kok's photosynthetic water oxidation clock, Nature 563 (7731) (2018) 421–425.
- [11] G. Renger, Mechanism of light induced water splitting in Photosystem II of oxygen evolving photosynthetic organisms, Biochim. Biophys. Acta Bioenerg. 1817 (8) (2012) 1164–1176.
- [12] J.D. Blakemore, R.H. Crabtree, G.W. Brudvig, Molecular Catalysts for Water Oxidation, Chem. Rev. 115 (23) (2015) 12974–13005.
- [13] B.M. Hunter, H.B. Gray, A.M. Muller, Earth-Abundant Heterogeneous Water Oxidation Catalysts, Chem. Rev. 116 (22) (2016) 14120–14136.
- [14] M. Okamura, M. Kondo, R. Kuga, Y. Kurashige, T. Yanai, S. Hayami, V.K. K. Praneeth, M. Yoshida, K. Yoneda, S. Kawata, S. Masaoka, A pentanuclear iron catalyst designed for water oxidation. Nature 530 (7591) (2016) 465–468.
- [15] M. Yagi, M. Kaneko, Molecular catalysts for water oxidation, Chem. Rev. 101 (1) (2001) 21–35.
- [16] M. Kondo, S. Masaoka, Water Oxidation Catalysts Constructed by Biorelevant Firstrow Metal Complexes, Chem. Lett. 45 (11) (2016) 1220–1231.
- [17] L. Zhang, M.S. Seo, Y. Choi, R. Ezhov, O. Maximova, D.D. Malik, M. Ng, Y.-M. Lee, R. Sarangi, Y.N. Pushkar, K.-B. Cho, W. Nam, A Manganese Compound I Model with a High Reactivity in the Oxidation of Organic Substrates and Water, J. Am. Chem. Soc. 145 (15) (2023) 8319–8325.
- [18] Y. Li, Y. Sun, Y. Qin, W. Zhang, L. Wang, M. Luo, H. Yang, S. Guo, Recent Advances on Water-Splitting Electrocatalysis Mediated by Noble-Metal-Based Nanostructured Materials, Adv. Energy Mater. 10 (11) (2020) 1903120.
- [19] P. Garrido-Barros, C. Gimbert-Surinach, R. Matheu, X. Sala, A. Llobet, How to make an efficient and robust molecular catalyst for water oxidation, Chem. Soc. Rev. 46 (20) (2017) 6088–6098.
- [20] Y. Pineda-Galvan, A.K. Ravari, S. Shmakov, L. Lifshits, N. Kaveevivitchai, R. Thummel, Y. Pushkar, Detection of the site protected 7-coordinate RuV = O species and its chemical reactivity to enable catalytic water oxidation, J. Catal. 375 (2019) 1–7.
- [21] R. Ezhov, A.K. Ravari, A. Page, Y. Pushkar, Water Oxidation Catalyst cis-[Ru(bpy) (5,5 '-dcbpy)(H2O)(2)](2+) and Its Stabilization in Metal-Organic Framework, ACS Catal. 10 (9) (2020) 5299–5308.
- [22] R. Ezhov, A.K. Ravari, Y. Pushkar, Characterization of the Fe-V=O Complex in the Pathway of Water Oxidation, Angew. Chem.-Int. Edit. 59 (32) (2020) 13502–13505.
- [23] R. Ezhov, A.K. Ravari, G. Bury, P.F. Smith, Y. Pushkar, Do multinuclear 3d metal catalysts achieve O-O bond formation via radical coupling or via water nucleophilic attack? WNA leads the way in [Co4O4]n+, Chem Catalysis 1 (2) (2021) 407–422.
- [24] D. Moonshiram, J.W. Jurss, J.J. Concepcion, T. Zakharova, I. Alperovich, T. J. Meyer, Y. Pushkar, Structure and electronic configurations of the intermediates of water oxidation in blue ruthenium dimer catalysis, J. Am. Chem. Soc. 134 (10) (2012) 4625–4636.
- [25] X.-Z. Wei, T.-Y. Ding, Y. Wang, B. Yang, Q.-Q. Yang, S. Ye, C.-H. Tung, L.-Z. Wu, Tracking an FeV(O) Intermediate for Water Oxidation in Water, Angew. Chem. Int. Ed. 62 (36) (2023) e202308192.
- [26] D. Moonshiram, I. Alperovich, J.J. Concepcion, T.J. Meyer, Y. Pushkar, Experimental demonstration of radicaloid character in a Ru-V=O intermediate in catalytic water oxidation, Proc. Natl. Acad. Sci. u. s. a. 110 (10) (2013) 3765–3770.
- [27] I. Prat, J.S. Mathieson, M. Güell, X. Ribas, J.M. Luis, L. Cronin, M. Costas, Observation of Fe(V)=O using variable-temperature mass spectrometry and its enzyme-like C-H and C=C oxidation reactions, Nat. Chem. 3 (10) (2011) 788–793.
- [28] X.-X. Li, S.-S. Xue, X. Lu, M.S. Seo, Y.-M. Lee, W.-S. Kim, K.-B. Cho, W. Nam, Ligand Architecture Perturbation Influences the Reactivity of Nonheme Iron(V)-Oxo Tetraamido Macrocyclic Ligand Complexes: A Combined Experimental and Theoretical Study, Inorg. Chem. 60 (6) (2021) 4058–4067.

- [29] B.M. Hunter, N.B. Thompson, A.M. Müller, G.R. Rossman, M.G. Hill, J.R. Winkler, H.B. Gray, Trapping an Iron(VI) Water-Splitting Intermediate in Nonaqueous Media, Joule 2 (4) (2018) 747–763.
- [30] F. Acuña-Parés, Z. Codolà, M. Costas, J.M. Luis, J. Lloret-Fillol, Unraveling the Mechanism of Water Oxidation Catalyzed by Nonheme Iron Complexes, Chem. -Eur. J. 20 (19) (2014) 5696–5707.
- [31] J.L. Fillol, Z. Codola, I. Garcia-Bosch, L. Gomez, J.J. Pla, M. Costas, Efficient water oxidation catalysts based on readily available iron coordination complexes, Nat. Chem. 3 (10) (2011) 807–813.
- [32] A. Das, J.E. Nutting, S.S. Stahl, Electrochemical C-H oxygenation and alcohol dehydrogenation involving Fe-oxo species using water as the oxygen source, Chem. Sci. 10 (32) (2019) 7542–7548.
- [33] M. Borrell, E. Andris, R. Navrátil, J. Roithová, M. Costas, Characterized cis-FeV(O) (OH) intermediate mimics enzymatic oxidations in the gas phase, Nat. Commun. 10 (1) (2019) 901.
- [34] J. Hohenberger, K. Ray, K. Meyer, The biology and chemistry of high-valent iron-oxo and iron-nitrido complexes, Nat. Commun. (2012,) 3.
- [35] N. Cox, M. Retegan, F. Neese, D.A. Pantazis, A. Boussac, W. Lubitz, Electronic structure of the oxygenevolving complex in photosystem II prior to O-O bond formation, Science 345 (6198) (2014) 804–808.
- [36] Y. Pushkar, Y. Pineda-Galvan, A.K. Ravari, T. Otroshchenko, D.A. Hartzler, Mechanism for O-O bond formation via radical coupling of metal and ligand based radicals – a new pathway, J. Am. Chem. Soc. 140 (42) (2018) 13538–13541.
- [37] K.M. Davis, B.T. Sullivan, M.C. Palenik, L. Yan, V. Purohit, G. Robison, I. Kosheleva, R.W. Henning, G.T. Seidler, Y. Pushkar, Rapid Evolution of the Photosystem II Electronic Structure during Water Splitting, Phys. Rev. X 8 (4) (2018), 041014.
- [38] P.E.M. Siegbahn, O-O bond formation in the S-4 state of the oxygen-evolving complex in photosystem II, Chem.- Eur. J. 12 (36) (2006) 9217–9227.
- [39] D.A. Pantazis, Missing Pieces in the Puzzle of Biological Water Oxidation, ACS Catal. 8 (10) (2018) 9477–9507.
- [40] A. Mishra, J. Yano, Y. Pushkar, V.K. Yachandra, K.A. Abboud, G. Christou, Heteronuclear MnCa/Sr Model Complexes, and Ca/Sr EXAFS Spectral Comparisons with the Oxygen-Evolving Complex of Photosystem II, Chem. Commun. 15 (2007) 1538–1540.
- [41] H.B. Lee, A.A. Shiau, D.A. Marchiori, P.H. Oyala, B.-K. Yoo, J.T. Kaiser, D.C. Rees, R.D. Britt, T. Agapie, CaMn3IVO4 Cubane Models of the Oxygen-Evolving Complex: Spin Ground States S<9/2 and the Effect of Oxo Protonation, Angew. Chem. Int. Ed. 60 (32) (2021) 17671–17679.
- [42] M. Kondo, S. Masaoka, Pentanuclear Scaffold: A Molecular Platform for Small-Molecule Conversions, Acc. Chem. Res. 53 (10) (2020) 2140–2151.
- [43] R.-Z. Liao, S. Masaoka, P.E.M. Siegbahn, Metal Oxidation States for the O-O Bond Formation in the Water Oxidation Catalyzed by a Pentanuclear Iron Complex, ACS Catal. 8 (12) (2018) 11671–11678.
- [44] C.N. Brodsky, R.G. Hadt, D. Hayes, B.J. Reinhart, N. Li, L.X. Chen, D.G. Nocera, In situ characterization of cofacial Co(IV) centers in Co404 cubane: Modeling the high-valent active site in oxygen-evolving catalysts, Proc. Nat. Acad. Sci. u. s. a. 114 (15) (2017) 3855–3860
- [45] H. Liu, H. Frei, Observation of O-O Bond Forming Step of Molecular Co4O4 Cubane Catalyst for Water Oxidation by Rapid-Scan FT-IR Spectroscopy, ACS Catal. 10 (3) (2020) 2138–2147.
- [46] R. Ezhov, A.K. Ravari, M. Palenik, A. Loomis, D.M. Meira, S. Savikhin, Y. Pushkar, Photoexcitation of Fe(3) O Nodes in MOF Drives Water Oxidation at pH=1 When Ru Catalyst Is Present, ChemSusChem 16 (5) (2023) e202202124.
- [47] L. Liu, S. Du, X. Guo, Y. Xiao, Z. Yin, N. Yang, Y. Bao, X. Zhu, S. Jin, Z. Feng, F. Zhang, Water-Stable Nickel Metal-Organic Framework Nanobelts for Cocatalyst-Free Photocatalytic Water Splitting to Produce Hydrogen, J. Am. Chem. Soc. 144 (6) (2022) 2747–2754.
- [48] E. Gouré, B. Gerey, M. Clémancey, J. Pécaut, F. Molton, J.-M. Latour, G. Blondin, M.-N. Collomb, Intramolecular Electron Transfers Thwart Bistability in a Pentanuclear Iron Complex, Inorg. Chem. 55 (18) (2016) 9178–9186.
- [49] S. Emamian, K.A. Ireland, V. Purohit, K.L. McWhorter, O. Maximova, W. Allen, S. Jensen, D.M. Casa, Y. Pushkar, K.M. Davis, X-ray Emission Spectroscopy of Single Protein Crystals Yields Insights into Heme Enzyme Intermediates, J. Phys. Chem. Lett. 14 (1) (2023) 41–48.
- [50] P. Glatzel, U. Bergmann, High resolution 1s core hole X-ray spectroscopy in 3d transition metal complexes—electronic and structural information, Coord. Chem. Rev. 249 (1–2) (2005) 65–95.
- [51] S. Lafuerza, A. Carlantuono, M. Retegan, P. Glatzel, Chemical Sensitivity of $K\beta$ and $K\alpha$ X-ray Emission from a Systematic Investigation of Iron Compounds, Inorg. Chem. 59 (17) (2020) 12518–12535.
- [52] S.D. Gamblin, D.S. Urch, Metal Kβ X-ray emission spectra of first row transition metal compounds, J. Electron Spectrosc. Relat. Phenom. 113 (2–3) (2001) 179–192.
- [53] D. Lebedev, R. Ezhov, J. Heras-Domingo, A. Comas-Vives, N. Kaeffer, M. Willinger, X. Solans-Monfort, X. Huang, Y. Pushkar, C. Coperet, Atomically Dispersed Iridium on Indium Tin Oxide Efficiently Catalyzes Water Oxidation, ACS Central Sci. 6 (7) (2020) 1189–1198.
- [54] J. Timoshenko, B. Roldan Cuenya, In Situ/Operando Electrocatalyst Characterization by X-ray Absorption Spectroscopy, Chem. Rev. 121 (2) (2021) 822 061
- [55] T.P. Keane, D.G. Nocera, Selective Production of Oxygen from Seawater by Oxidic Metallate Catalysts, ACS Omega 4 (7) (2019) 12860–12864.
- [56] S. Lin, Y. Pineda-Galvan, W.A. Maza, C.C. Epley, J. Zhu, M.C. Kessinger, Y. Pushkar, A.J. Morris, Electrochemical Water Oxidation by a Catalyst-Modified Metal-Organic Framework Thin Film, ChemSusChem 10 (3) (2017) 514–522.

- [57] H. Dau, P. Liebisch, M. Haumann, X-ray absorption spectroscopy to analyze nuclear geometry and electronic structure of biological metal centers - Potential and questions examined with special focus on the tetra-nuclear manganese complex of oxygenic photosynthesis, Anal. Bioanal. Chem. 376 (5) (2003) 562–583.
- [58] F.T. de Oliveira, A. Chanda, D. Banerjee, X.P. Shan, S. Mondal, L. Que, E. L. Bominaar, E. Munck, T.J. Collins, Chemical and spectroscopic evidence for an Fe-V-Oxo complex, Science 315 (5813) (2007) 835–838.
- [59] J. England, Y. Guo, E.R. Farquhar, V.G. Young Jr, E. Münck, L. Que Jr, The Crystal Structure of a High-Spin Oxoiron(IV) Complex and Characterization of Its Self-Decay Pathway, J. Am. Chem. Soc. 132 (25) (2010) 8635–8644.
- [60] P.J. Riggs-Gelasco, J.C. Price, R. B. Guyer, J.H. Brehm, E.W. Barr, J. M. Bollinger Jr., C. Krebs, EXAFS Spectroscopic Evidence for an Fe=O Unit in the Fe(IV) Intermediate Observed during Oxygen Activation by Taurine:α-Ketoglutarate Dioxygenase. J. Am. Chem. Soc. 2004, 126 (26), 8108-8109.
- [61] M.I. Scullane, L.K. White, N.D. Chasteen, An efficient approach to computer simulation of EPR spectra of high-spin Fe(III) in rhombic ligand fields, J. Magnetic Reson (1969) 47 (3) (1982) 383–397.
- [62] R. Cammack, C.E Cooper., [12] Electron paramagnetic resonance spectroscopy of iron complexes and iron-containing proteins. In *Methods in Enzymology*, Academic Press: 1993; Vol. 227, pp 353-384.
- [63] Transition-Group Ions. In Electron Paramagnetic Resonance, 2006; pp 225-252.
- [64] N.E. Holubowitch, G. Nguyen, Dimerization of [FeIII(bpy)3]3+ in Aqueous Solutions: Elucidating a Mechanism Based on Historical Proposals, Electrochemical Data, and Computational Free Energy Analysis, Inorg. Chem. 61 (25) (2022) 9541–9556.
- [65] V.K. Voronkova, J. Mrozinski, M.A. Yampolskaya, Y.V. Yablokov, N.S. Evtushenko, M.S. Byrke, N.V. Gerbeleu, MIXED-VALENCE FE(III)-FE(IV) DIMERS PREPARATION AND PHYSICAL-PROPERTIES OF OXIDATION-PRODUCTS OF OXO-BRIDGED BINUCLEAR IRON(III) COMPLEXES, Inorg. Chim. Acta 238 (1–2) (1995) 139–147.
- [66] N. Mitić, M.D. Clay, L. Saleh, J.M. Bollinger, E.I. Solomon, Spectroscopic and Electronic Structure Studies of Intermediate X in Ribonucleotide Reductase R2 and Two Variants: A Description of the FeIV-Oxo Bond in the FeIII-O-FeIV Dimer, J. Am. Chem. Soc. 129 (29) (2007) 9049–9065.
- [67] K. Meyer, E. Bill, B. Mienert, T. Weyhermüller, K. Wieghardt, Photolysis of cis- and trans-[FeIII(cyclam)(N3)2]+ Complexes: Spectroscopic Characterization of a Nitridoiron(V) Species, J. Am. Chem. Soc. 121 (20) (1999) 4859–4876.
- [68] T. Jüstel, T. Weyhermüller, K. Wieghardt, E. Bill, M. Lengen, A.X. Trautwein, P. Hildebrandt, µ-Nitridodiiron Complexes with Asymmetric [FeIV N-FeIII]4+ and Symmetric [FeIV N FeIV]5+ Structural Elements, Angew. Chem. Int. Ed. 34 (6) (1995) 669–672.
- [69] T. Jüstel, M. Müller, T. Weyhermüller, C. Kressl, E. Bill, P. Hildebrandt, M. Lengen, M. Grodzicki, A.X. Trautwein, B. Nuber, K. Wieghardt, The Molecular and Electronic Structure of Symmetrically and Asymmetrically Coordinated, Non-Heme Iron Complexes Containing [FeIII(μ-N)FeIV]4+ (S=3/2) and [FeIV(μ-N)FeIV]5+ (S=0) Cores. Chem. Fur. J. 5 (2) (1999) 793-810.
- [70] M. Dan-Hardi, H. Chevreau, T. Devic, P. Horcajada, G. Maurin, G. Férey, D. Popov, C. Riekel, S. Wuttke, J.-C. Lavalley, A. Vimont, T. Boudewijns, D. de Vos, C. Serre, How Interpenetration Ensures Rigidity and Permanent Porosity in a Highly Flexible Hybrid Solid. Chem. Mater. 24 (13) (2012) 2486–2492.
- [71] P. Railey, Y. Song, T. Liu, Y. Li, Metal organic frameworks with immobilized nanoparticles: Synthesis and applications in photocatalytic hydrogen generation and energy storage, Mater. Res. Bull. 96 (2017) 385–394.
- [72] J. De Decker, K. Folens, J. De Clercq, M. Meledina, G. Van Tendeloo, G. Du Laing, P. Van Der Voort, Ship-in-a-bottle CMPO in MIL-101(Cr) for selective uranium recovery from aqueous streams through adsorption, J. Hazard. Mater. 335 (2017)
- [73] D. Bara, C. Wilson, M. Mörtel, M.M. Khusniyarov, S. Ling, B. Slater, S. Sproules, R. S. Forgan, Kinetic Control of Interpenetration in Fe–Biphenyl-4,4'-dicarboxylate Metal-Organic Frameworks by Coordination and Oxidation Modulation, J. Am. Chem. Soc. 141 (20) (2019) 8346–8357.
- [74] P. Pelosin, M. Gil-Sepulcre, P. Garrido-Barros, D. Moonshiram, J. Benet-Buchholz, C. Gimbert-Suriñach, A. Llobet, Analysis of the Active Species Responsible for Water Oxidation Using a Pentanuclear Fe Complex. iScience 2020, 23 (8), 101378.
- [75] L. Vicens, G. Olivo, M. Costas, Rational Design of Bioinspired Catalysts for Selective Oxidations, ACS Catal. 10 (15) (2020) 8611–8631.
- [76] A.H. Proppe, Y.C. Li, A. Aspuru-Guzik, C.P. Berlinguette, C.J. Chang, R. Cogdell, A. G. Doyle, J. Flick, N.M. Gabor, R. van Grondelle, S. Hammes-Schiffer, S.A. Jaffer, S. O. Kelley, M. Leclerc, K. Leo, T.E. Mallouk, P. Narang, G.S. Schlau-Cohen, G. D. Scholes, A. Vojvodic, V.-W.-W. Yam, J.Y. Yang, E.H. Sargent, Bioinspiration in light harvesting and catalysis, Nat. Rev. Mater. 5 (11) (2020) 828–846.
- [77] H. Xu, D. Cheng, D. Cao, X.C. Zeng, A universal principle for a rational design of single-atom electrocatalysts, Nat. Catal. 1 (5) (2018) 339–348.
- [78] Y. Wang, L. Xiao, Y. Qi, M. Mahmoodinia, X. Feng, J. Yang, Y.-A. Zhu, D. Chen, Towards rational catalyst design: boosting the rapid prediction of transition-metal activity by improved scaling relations, Phys. Chem. Chem. Phys. 21 (35) (2019) 19269–19280.
- [79] N.S.R. McCool, D. M.; Sheats, J. E.; Dismukes, G. C., A Co4O4 "Cubane" Water Oxidation Catalyst Inspired by Photosynthesis. J. Am. Chem. Soc. 2011, 133 (30), 11446-11449.
- [80] C. Panda, J. Debgupta, D.D. Diaz, K.K. Singh, S.S. Gupta, B.B. Dhar, Homogeneous Photochemical Water Oxidation by Biuret-Modified Fe-TAML: Evidence of Fe-V(O) Intermediate, J. Am. Chem. Soc. 136 (35) (2014) 12273–12282.
- [81] S. Pattanayak, D.R. Chowdhury, B. Garai, K.K. Singh, A. Paul, B.B. Dhar, S. Sen Gupta, Electrochemical Formation of Fe-V(O) and Mechanism of Its Reaction with Water During O-O Bond Formation, Chem. - Eur. J. 23 (14) (2017) 3414–3424.

- [82] L. Chen, Q. Xu, Metal-Organic Framework Composites for Catalysis, Matter 1 (1) (2019) 57–89.
- [83] G. Lu, S. Li, Z. Guo, O.K. Farha, B.G. Hauser, X. Qi, Y. Wang, X. Wang, S. Han, X. Liu, J.S. DuChene, H. Zhang, Q. Zhang, X. Chen, J. Ma, S.C.J. Loo, W.D. Wei, Y. Yang, J.T. Hupp, F. Huo, Imparting functionality to a metal-organic framework material by controlled nanoparticle encapsulation, Nat. Chem. 4 (4) (2012) 310–316.
- [84] E. Gkaniatsou, C. Sicard, R. Ricoux, L. Benahmed, F. Bourdreux, Q. Zhang, C. Serre, J.-P. Mahy, N. Steunou, Enzyme Encapsulation in Mesoporous Metal-Organic Frameworks for Selective Biodegradation of Harmful Dye Molecules, Angew. Chem. Int. Ed. 57 (49) (2018) 16141–16146.
- [85] H. Zheng, Y. Zhang, L. Liu, W. Wan, P. Guo, A.M. Nyström, X. Zou, One-pot Synthesis of Metal-Organic Frameworks with Encapsulated Target Molecules and Their Applications for Controlled Drug Delivery, J. Am. Chem. Soc. 138 (3) (2016) 962–968.
- [86] B. Nepal, S. Das, Sustained Water Oxidation by a Catalyst Cage-Isolated in a Metal-Organic Framework, Angew. Chem.-Int. Edit. 52 (28) (2013) 7224–7227.
- [87] Y. Horiuchi, T. Toyao, K. Miyahara, L. Zakary, D.D. Van, Y. Kamata, T.-H. Kim, S. W. Lee, M. Matsuoka, Visible-light-driven photocatalytic water oxidation catalysed by iron-based metal-organic frameworks, Chem. Commun. 52 (29) (2016) 5190-5193
- [88] S. Emamian, K.A. Ireland, V. Purohit, K.L. McWhorter, O. Maximova, W. Allen, S. Jensen, D.M. Casa, Y. Pushkar, K.M. Davis, X-ray Emission Spectroscopy of

- Single Protein Crystals Yields Insights into Heme Enzyme Intermediates, J. Phys. Chem. Lett. 14 (2022) 41–48.
- [89] I.-H. Hwang, M.A. Solovyev, S.-W. Han, M.K.Y. Chan, J.P. Hammonds, S.M. Heald, S.D. Kelly, N. Schwarz, X. Zhang, C.-J. Sun, AXEAP: a software package for X-ray emission data analysis using unsupervised machine learning, J Synchrotron Radiat 29 (5) (2022) 1309–1317.
- [90] A.D. Becke, Density-functional exchange-energy approximation with correct asymptotic behavior, Phys. Rev. A 38 (6) (1988) 3098–3100.
- [91] J.P. Perdew, W. Yue, Accurate and simple density functional for the electronic exchange energy: Generalized gradient approximation, Phys. Rev. B 33 (12) (1986) 8800–8802.
- [92] Y. Pushkar, D. Moonshiram, V. Purohit, L. Yan, I. Alperovich, Spectroscopic Analysis of Catalytic Water Oxidation by [RuII(bpy)(tpy)H2O]2+ Suggests That RuV=O Is Not a Rate-Limiting Intermediate, J. Am. Chem. Soc. 136 (34) (2014) 11938–11945.
- [93] D. Moonshiram, Y. Pineda-Galvan, D. Erdman, M. Palenik, R.F. Zong, R. Thummel, Y. Pushkar, Uncovering the Role of Oxygen Atom Transfer in Ru-Based Catalytic Water Oxidation, J. Am. Chem. Soc. 138 (48) (2016) 15605–15616.
- [94] G. Bury, Y. Pushkar, Computational Analysis of Structure-Activity Relationships in Highly Active Homogeneous Ruthenium—Based Water Oxidation Catalysts, Catalysts 12 (8) (2022) 863.